
INTERNAL WAVES GENERATED BY A VORTEX PAIR

Gary S. Lapham
John P. McHugh

Northeast Consortium for Engineering Education
68 Port Royal Square
Port Royal, VA 22535

September 1999

Scientific Report

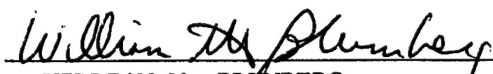
APPROVED FOR PUBLIC RELEASE; DISTRIBUTION IS UNLIMITED.

20020624 084

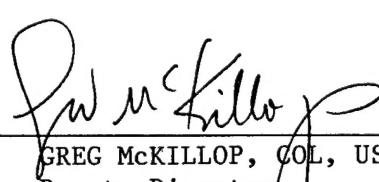


AIR FORCE RESEARCH LABORATORY
Space Vehicles Directorate
29 Randolph Road
AIR FORCE MATERIEL COMMAND
HANSOM AIR FORCE BASE MA 01731-3010

"This technical report has been reviewed and is approved for publication"



WILLIAM M. BLUMBERG
Contract Manager



GREG MCKILLOP, COL, USAF
Deputy Director
Battlespace Environment Div

This report has been reviewed by the ESC Public Affairs Office (PA) and is releasable to the National Technical Information Service (NTIS).

Qualified requestors may obtain additional copies from the Defense Technical Information Center (DTIC). All others should apply to the National Technical Information Service (NTIS).

If your address has changed, if you wish to be removed from the mailing list, or if the addressee is no longer employed by your organization, please notify AFRL/VSIM, 29 Randolph Road, Hanscom AFB MA 01731-3010. This will assist us in maintaining a current mailing list.

Do not return copies of this report unless contractual obligations or notices on a specific document require that it be returned.

REPORT DOCUMENTATION PAGE

Form Approved
OMB No. 0704-0188

Public reporting burden for this collection of information is estimated to average 1 hour per response, including the time for reviewing instructions, searching existing data sources, gathering and maintaining the data needed, and completing and reviewing this collection of information. Send comments regarding this burden estimate or any other aspect of this collection of information, including suggestions for reducing burden, to Department of Defense, Washington Headquarters Services, Directorate for Information Operations and Reports (0704-0188), 1215 Jefferson Davis Highway, Suite 1204, Arlington, VA 22202-4302. Respondents should be aware that notwithstanding any other provision of law, no person shall be subject to any penalty for failing to comply with a collection of information if it does not display a currently valid OMB control number. PLEASE DO NOT RETURN YOUR FORM TO THE ABOVE ADDRESS.

1. REPORT DATE (DD-MM-YYYY)	2. REPORT TYPE		3. DATES COVERED (From - To)		
07 Sep 99	Interim				
4. TITLE AND SUBTITLE			5a. CONTRACT NUMBER		
Internal Waves Generated by a Vortex Pair			F19628-98-C-0029		
			5b. GRANT NUMBER		
			5c. PROGRAM ELEMENT NUMBER		
			62101F		
6. AUTHOR(S)			5d. PROJECT NUMBER		
Gary Lapham and *John McHugh			9993		
			5e. TASK NUMBER		
			GS		
			5f. WORK UNIT NUMBER		
			PE		
7. PERFORMING ORGANIZATION NAME(S) AND ADDRESS(ES)			8. PERFORMING ORGANIZATION REPORT NUMBER		
Northeast Consortium for Engineering Education, 68 Port Royal Square, Port Royal VA 22535					
* University of New Hampshire, 134 Kingsbury Hall, Durham, NH 03834					
9. SPONSORING / MONITORING AGENCY NAME(S) AND ADDRESS(ES)			10. SPONSOR/MONITOR'S ACRONYM(S)		
Air Force Research Laboratory/VSB 29 Randolph Road Hanscom AFB MA 01731-3010					
			11. SPONSOR/MONITOR'S REPORT NUMBER(S)		
			AFRL-VS-TR-2002-1560		
12. DISTRIBUTION / AVAILABILITY STATEMENT					
Approved for public release: distribution unlimited					
13. SUPPLEMENTARY NOTES					
14. ABSTRACT					
<p>Both observations and direct numerical simulations have shown that convecting storms create significant internal gravity wave activity. However, the physical mechanism for gravity wave generation is not clear. In this work, numerical simulations of a simple vortex model of convection have been performed for three different cases: a constant density case; a constant Brunt-Vasala frequency case; and a case with two layers, each with its own Brunt-Vasala frequency.</p>					
15. SUBJECT TERMS					
Phillips Laboratory Scholar Program, convective storms, gravity waves, vortex model, numerical simulation					
16. SECURITY CLASSIFICATION OF:			17. LIMITATION OF ABSTRACT	18. NUMBER OF PAGES	19a. NAME OF RESPONSIBLE PERSON
a. REPORT unclassified	b. ABSTRACT unclassified	c. THIS PAGE unclassified	unlimited	34	William A.M. Blumberg
					19b. TELEPHONE NUMBER (include area code) 781-377-3601

1 Introduction

Observations have shown that convecting storms create significant internal wave activity; see for example the recent satellite observations of Dewan, et al [1]. Direct numerical simulations [2, 3, 4, 5] also have identified convective storms as a source of gravity waves. There is little doubt that convection creates wave energy in the atmosphere. Internal waves in the atmosphere may be created by other phenomena, as well as convection. The other phenomena most often blamed for wavemaking are jet streams, fronts, and flow over mountains. The relative importance of the different wave sources is a topic of current debate.

The mechanism of gravity wave generation by convecting storms is not clear. Clark [2] claims there are two mechanisms. The first mechanism concerns the zonal flow (average horizontal flow) that usually exists in the atmosphere. Convection acts as an obstruction to this flow, deflecting the airflow over and around the thunderstorm, analogous to flow over a mountain. This obstruction creates a pattern of steady waves, analogous to mountain waves.

The second mechanism concerns an oscillation of the flow inside a thunderstorm, which can act as a mechanical wavemaker. Fovell, et al, [4] studied the second mechanism using an artificial mechanical oscillator in a realistic atmosphere. The results of Fovell are two-dimensional direct numerical simulations. Fovell found that the simple mechanical oscillator created a fixed V-shaped pattern of waves. Fovell showed that the wave pattern is largely influenced by the zonal shear flow, and by the orientation of the mechanical oscillator. They argue that the stratospheric waves apparent in the simulations are the result of an interaction between the convection and the tropopause. Realistic simulations of convecting storms have also been performed by Lane, et al [3], and Holton and Alexander [5]. The V-shaped wave pattern is clearly evident in both sets of results, similar to the waves produced by Fovell.

Numerical simulations of a simple model of convection are considered below. The simulations are restricted to two spatial dimensions. The convection is modeled as a vortex pair, scaled to match the typical size and strength of a real convecting storm. However, the tremendous complexity of an actual storm is not included. Instead, by

including only the simple model of the large scale flow, and the resulting gravity wave activity, the relationship between convection and waves is more easily understood.

Previous numerical simulations by Hill [6] also considered a vortex pair in a stratified fluid. Waves are not mentioned in Hill's work, and the results focus on the movement of the center of the vortex. The size and strength of the vortices of Hill were chosen to represent the motion of trailing vortices behind an aircraft, rather than the large scale motion of storms. The stratification is weak when considering an aircraft's trailing vortex. The scale of a convecting storm is large, and the stratification is relatively strong, which accounts for the difference between Hill's results and the results given below.

The equations treated here are the anelastic equations. The anelastic equations model the dynamics of an adiabatic atmosphere approximately, and do not allow sound wave propagation. The lack of sound waves does not seriously affect the dynamics of the internal waves, but does allow a significantly larger time step when compared to a numerical model of the fully compressible equations. The anelastic equations were first suggested by Batchelor [7], and then further developed by several authors [8],[9],[10]. The original anelastic equations have a flaw; the linear solution does not match the linear solution of the fully compressible equations. It was later shown that the pressure term was incorrect. Bacmeister and Schoeberl [11] provide a concise derivation of the corrected anelastic equations.

The numerical method is spectral in space with periodic sidewall boundaries, and rigid boundaries on the top and bottom. A wave damping layer is also included near the top boundary. The temporal algorithm is semi-implicit, and uses a formulation where the pressure and the horizontal velocity are eliminated from the linear terms in the equations. Details are provided by McHugh [12].

Three base states are considered; a constant density case, a constant Brunt-Vaisala case, and a case with two layers, each with its own constant value of the Brunt-Vaisala frequency. This last case models the atmosphere in the region of the tropopause.

2 Governing equations

Although the results given later are two dimensional, the equations and numerical methods are capable of three dimensions, and are developed here in three dimensions. The reduction to two dimensions is discussed where appropriate.

The anelastic equations for a compressible atmosphere are

$$\frac{Du}{Dt} = -\frac{\partial p^*}{\partial x} + \frac{1}{R_e} \nabla^2 u, \quad (1)$$

$$\frac{Dv}{Dt} = -\frac{L_x}{L_y} \frac{\partial p^*}{\partial y} + \frac{1}{R_e} \nabla^2 v, \quad (2)$$

$$\frac{Dw}{Dt} = -\frac{L_x}{L_z} \frac{\partial p^*}{\partial z} + \frac{1}{F_r^2 \bar{\theta}} + \frac{1}{R_e} \nabla^2 w, \quad (3)$$

$$\frac{D\theta}{Dt} + w \frac{L_x}{L_z} \frac{\partial \bar{\theta}}{\partial z} = \frac{1}{R_e P_r} \nabla^2 \theta, \quad (4)$$

$$\frac{\partial \bar{\rho} u}{\partial x} + \frac{L_x}{L_y} \frac{\partial \bar{\rho} v}{\partial y} + \frac{L_x}{L_z} \frac{\partial \bar{\rho} w}{\partial z} = 0, \quad (5)$$

where

$$p^* = \frac{c_p \bar{\theta}}{U^2} \left(\frac{p}{p_0} \right)^{\frac{R}{c_p}}, \quad (6)$$

$$\theta = T \left(\frac{p_0}{p} \right)^{\frac{R}{c_p}}, \quad (7)$$

$$\frac{D}{Dt} = \frac{\partial}{\partial t} + u \frac{\partial}{\partial x} + v \frac{L_x}{L_y} \frac{\partial}{\partial y} + w \frac{L_x}{L_z} \frac{\partial}{\partial z}, \quad (8)$$

$$\nabla^2 = \frac{\partial^2}{\partial x^2} + \frac{L_x^2}{L_y^2} \frac{\partial^2}{\partial y^2} + \frac{L_x^2}{L_z^2} \frac{\partial^2}{\partial z^2}, \quad (9)$$

u, v, w are the velocity components, x, y, z are the components of position, θ is the potential temperature, $\bar{\rho}$ and $\bar{\theta}$ are the basic state density and potential temperature, c_p is the specific heat at constant pressure, R is the gas constant, p is the pressure, and p_0 is a constant. Equations (1-3) are the momentum equations, (4) is the energy equation, and (5) is the continuity equation. They have been rescaled using a velocity scale, U , to be defined later, and a length scale, L , which is the horizontal length (parallel to the x direction) of the domain. Note that L_x, L_y , and L_z are length scale

ratios which account for the difference between the physical domain lengths and the computational domain lengths. The density and potential temperature are rescaled using their respective values at the bottom of the domain ($\bar{\rho}_0$, $\bar{\theta}_0$). The Reynolds, Prandtl, and Froude numbers are

$$R_e = \frac{UL}{\nu}, \quad (10)$$

$$P_r = \frac{\nu}{\kappa}, \quad (11)$$

$$F_r^2 = \frac{U^2}{gL}. \quad (12)$$

The basic state is governed by the perfect gas law,

$$\bar{p} = \bar{\rho}R\bar{T}, \quad (13)$$

and the equation of static equilibrium,

$$\frac{\partial \bar{p}}{\partial z} = -\bar{\rho}g. \quad (14)$$

Generally the base state temperature profile, \bar{T} , is chosen, and the remaining base state variables are determined using (7), (13), and (14).

One important base state parameter is the Brunt-Vaisala frequency, defined as

$$\frac{g}{\bar{\theta}} \frac{\partial \bar{\theta}}{\partial z}. \quad (15)$$

Rescaling this frequency as before gives the Brunt-Vaisala parameter:

$$N^2 = \frac{Lg}{U^2} \frac{1}{\bar{\theta}} \frac{\partial \bar{\theta}}{\partial z} = \frac{1}{F_r^2} \frac{1}{\bar{\theta}} \frac{\partial \bar{\theta}}{\partial z}, \quad (16)$$

where z is now dimensionless. Another base state parameter is the scale height,

$$\frac{1}{H} = -\frac{\bar{\rho}_z}{\bar{\rho}}, \quad (17)$$

3 The Numerical Scheme

The numerical method is that of McHugh [12]. It is similar to the normal velocity-normal vorticity method of Kim, Moin, and Moser [13], who studied the incompressible Navier-Stokes equations. The governing equations are reduced such that pressure and horizontal velocity components are eliminated from the linear terms, resulting in

$$\left[\frac{\partial}{\partial t} - \frac{1}{R_e} \nabla^2 \right] \left[\nabla^2 w - \frac{\partial}{\partial z} \left(\frac{1}{H} w \right) \right] - \frac{1}{F_r^2} \nabla_1^2 \bar{\theta} = \nabla^2 A_3 + \frac{\partial}{\partial z} \frac{\partial A_i}{\partial x_i}, \quad (18)$$

where A_i is the sum of the nonlinear terms for the i^{th} momentum equation,

$$A_i = u_j \frac{\partial u_i}{\partial x_j}, \quad (19)$$

and

$$\nabla_1^2 = \frac{\partial^2}{\partial x^2} + \frac{L_x^2}{L_y^2} \frac{\partial^2}{\partial y^2}. \quad (20)$$

The order of (18) is reduced by introducing ϕ :

$$\phi = \nabla^2 w - \frac{\partial}{\partial z} \left(\frac{1}{H} w \right). \quad (21)$$

Equation (18) then becomes

$$\frac{\partial \phi}{\partial t} - \frac{1}{R_e} \nabla^2 \phi - \frac{1}{F_r^2} \nabla_1^2 \bar{\theta} = \nabla^2 A_3 + \frac{\partial}{\partial z} \frac{\partial A_i}{\partial x_i}. \quad (22)$$

The variable ϕ is retained in the calculations, and w , ϕ , and θ are determined simultaneously using (21), (22), and the energy equation. The energy equation is now written as

$$\frac{\partial \theta}{\partial t} = -w \frac{\partial \bar{\theta}}{\partial z} - B, \quad (23)$$

where B is the sum of the nonlinear terms for the energy equation,

$$B = u_j \frac{\partial \theta}{\partial x_j}. \quad (24)$$

The boundary conditions are

$$w = w_z = \theta = 0 \quad (25)$$

on the rigid boundaries. Note that the sidewalls are treated with periodic boundary conditions, and no further enforcement is allowed.

After w , ϕ , and θ are found, the remaining task is to determine the horizontal velocity, u and v . There is a particularly straightforward method of finding the horizontal velocity in two dimensions. Keeping x as the horizontal direction and z as the vertical, the continuity equation is

$$u_x = - \left[w_z + \frac{\bar{\rho}_z}{\bar{\rho}} w \right]. \quad (26)$$

This equation is easily solved for u once w is available.

In three dimensions, the vorticity equation is necessary, along with the continuity equation, to determine both components of velocity. The vertical vorticity equation for viscous flow is

$$\frac{\partial \eta}{\partial t} = \frac{1}{R_e} \nabla^2 \eta + \frac{\partial A_2}{\partial x} - \frac{\partial A_1}{\partial y}, \quad (27)$$

where η is the vertical component of vorticity. The boundary condition on the rigid boundaries is

$$\eta = 0. \quad (28)$$

Equation (27) is solved for the vorticity, subject to (28), and then the definition of vorticity provides one equation for horizontal velocity:

$$u_y - v_x = \eta. \quad (29)$$

This result, along with the continuity equation,

$$u_x + v_y = - \left[w_z + \frac{\bar{\rho}_z}{\bar{\rho}} w \right], \quad (30)$$

are sufficient to determine u and v .

The spatial discretization is a spectral method. The horizontal directions are expanded in Fourier series. The vertical direction uses a spectral element method, using Lagrange interpolants within each subdomain, collocated on the Chebyshev-Gauss-Lobatto points. A damping layer is used at the top of the domain as a non-reflecting lid. Note that the damping layer is ineffective for gravity waves with wavelengths greater than the damping layer thickness.

4 Initial Conditions: A vortex pair

The initial conditions are a pair of point vortices. The velocity field for a point vortex is taken from the well-known similarity solution for a diffusing line vortex, as discussed in Sherman [14]. This similarity solution is an exact solution to the Navier-Stokes equations for constant density, viscous flow. In cylindrical coordinates, the velocity field for a single vortex located at the origin is

$$v = \frac{\Gamma}{2\pi r} \left[1 - e^{-\frac{r^2}{4\nu t}} \right], \quad (31)$$

where v is now the azimuthal velocity, r is the radial distance from the center of the vortex, Γ is the circulation around the vortex, and ν is the kinematic viscosity. The radial component of velocity is zero. This solution is rescaled using the same length and velocity scale as before. The resulting azimuthal velocity is

$$v = \frac{G}{2\pi r} \left[1 - e^{-\frac{Gr^2}{4t}} \right], \quad (32)$$

where v , r , and t are now dimensionless, and the dimensionless vortex strength is defined as

$$G = \frac{\Gamma}{LU}. \quad (33)$$

Note that the solution given by (32) depends on time as well as space. Only one value of time was used to start the simulations. The vortex was merely used to start a flow that has the general characteristics of the vortex pair being studied.

An obvious alternative to the viscous vortex is the well-known irrotational inviscid vortex. Simulations with the irrotational vortex led to numerical instabilities, clearly originating at the core, where the analytic solution is unbounded. Attempts to smooth the initial conditions at the core, and then advance the solution with the chosen spectral method, were tedious and only marginally successful. Hence the irrotational vortex was not pursued.

5 Results and Discussion

The flow is initiated by releasing a pair of counterrotating vortices in an otherwise motionless flow. The vortex pair is chosen to rotate with a downward velocity in the

Table 1: Dimensionless parameter values

Reynolds number	2000
Prandtl number	1
Froude number	1
Vortex strength	1
L_x / L_z	1

region between the vortices. This choice is based on the initiation of a storm event in the atmosphere, which is well-known to result in a downward wind in the storm center. The vortices are initially located at one quarter of the domain height from the bottom ($z=-0.5$), and a dimensionless distance of 1.0 from the horizontal center.

There is no zonal flow in the present simulations, which means that a velocity scale must be selected from other parameters. The velocity scale is chosen to be $U = \sqrt{gL}$, where g is the gravitational constant, and L is horizontal domain length. The Froude number becomes unity, the Prandtl number and the scale height are unchanged, and the other parameters are now

$$R = \frac{\sqrt{gL^3}}{\nu}, \quad (34)$$

$$G = \frac{\Gamma}{\sqrt{gL^3}}, \quad (35)$$

$$N^2 = \frac{1}{\bar{\theta}} \frac{\partial \bar{\theta}}{\partial z}. \quad (36)$$

Before discussing the results for the stratified case, it is useful to consider a flow without stratification. The base state density, potential temperature, and pressure are chosen to be constant, and the flow is started with the same initial conditions as the stratified case. Since the boundary conditions on temperature are homogeneous, and the initial temperature field is zero, the potential temperature remains zero throughout the simulation for this case. The total effect is that the equations are reduced to the incompressible Navier-Stokes equations. Table 1 lists the chosen dimensionless parameter values. Table 2 lists the physical parameter values on which

Figure 3: Surface plot of velocity magnitude for the constant density case with $t=1.0$

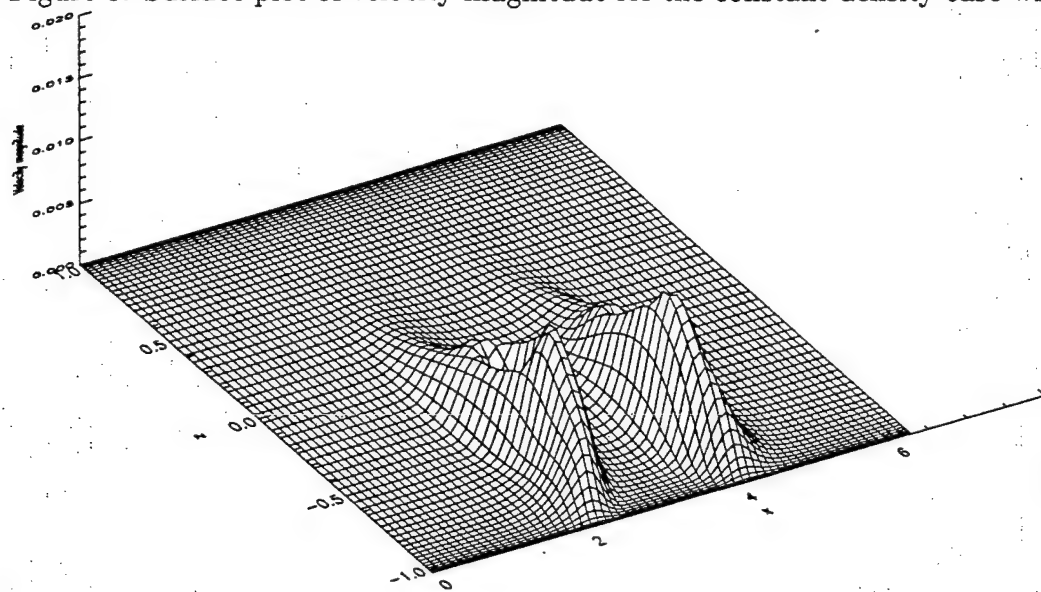


Figure 4: Surface plot of velocity magnitude for the constant density case with $t=32.0$

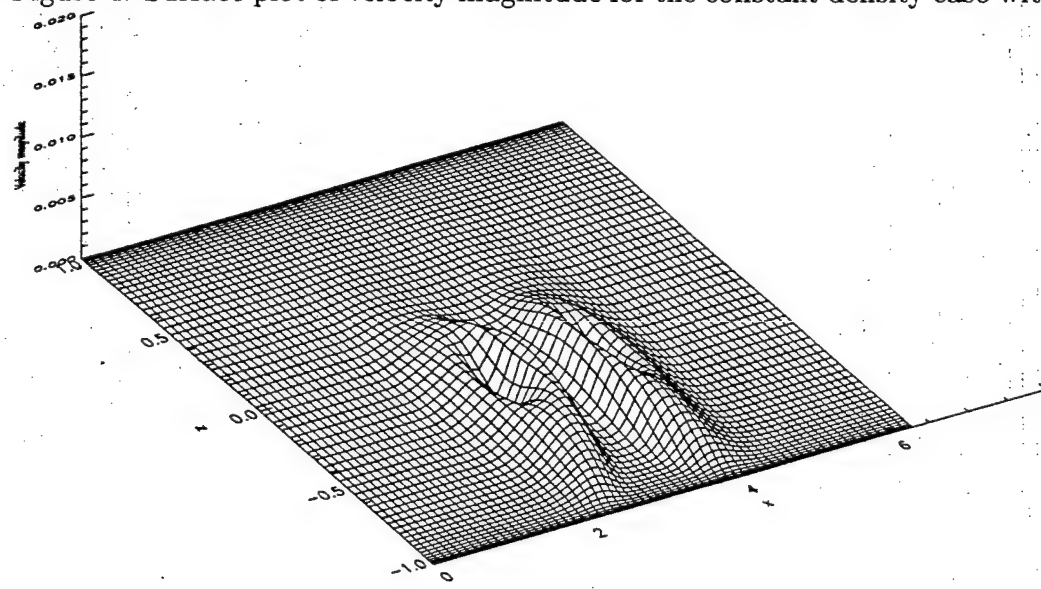


Figure 5: Contour plot of vorticity for the constant density case with $t=1.0$

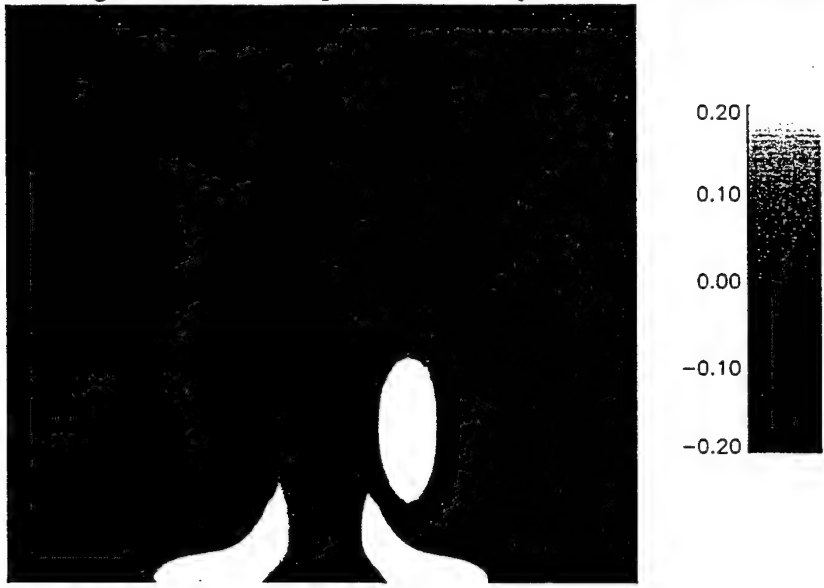


Figure 6: Contour plot of vorticity for the constant density case with $t=32.0$

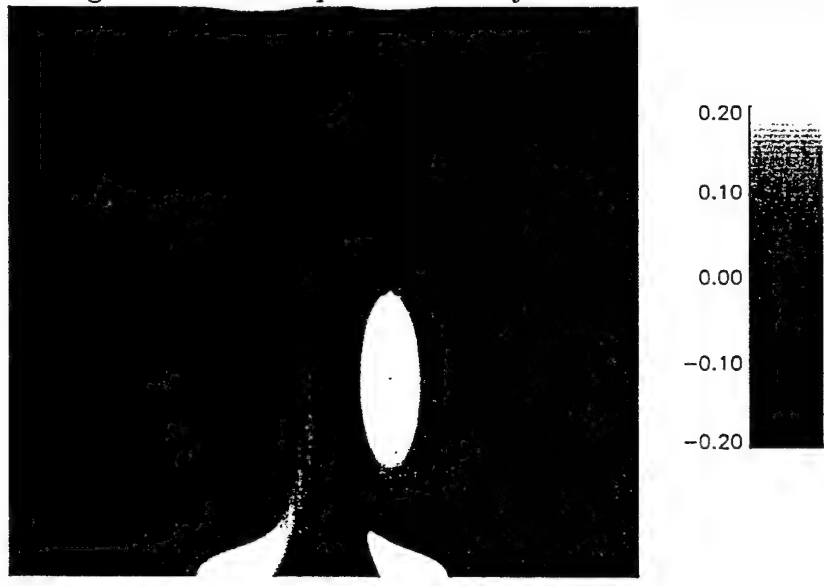
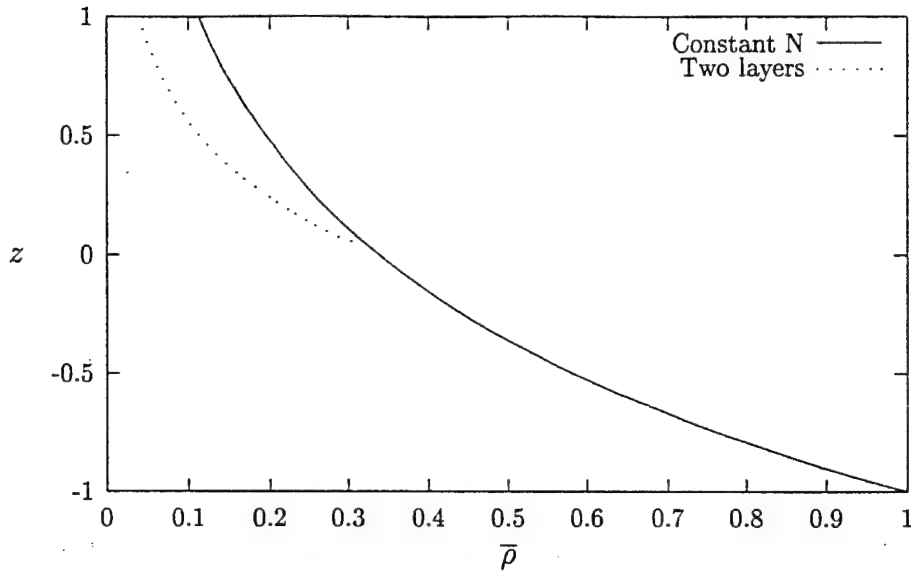


Figure 7: Base state density profiles



atively short time span of $t=32$ dimensionless units. The vortices move together slightly, reminiscent of the Bernoulli effect between two spinning cylinders. The vortices also decay in strength, and diffuse outward from the center of the vortex. The close proximity of the two vortices causes them to become elongated in the vertical, and to induce an upwards motion of the vortex pair. This vertically induced motion of a vortex pair is well-known, and is discussed in Lamb [15].

Now consider stratified flow. The base state is chosen to have a constant Brunt-Vaisala frequency, achieved with a linear variation in temperature. Figure 7 shows the base state density profile. The dimensionless parameter values are the same as those for the constant density case, as shown in Table 2, with the addition of the Brunt-Vaisala parameter value of 0.32.

The results of this stratified case are shown in figures 8-19, using the same combination of velocity vector plots, surface plots of the velocity magnitude, and colored contour plots of the vorticity.

The dynamics of the vortices in stratified flow are dramatically different than the

Figure 8: Velocity vector plot for the constant N case with $t=1.0$

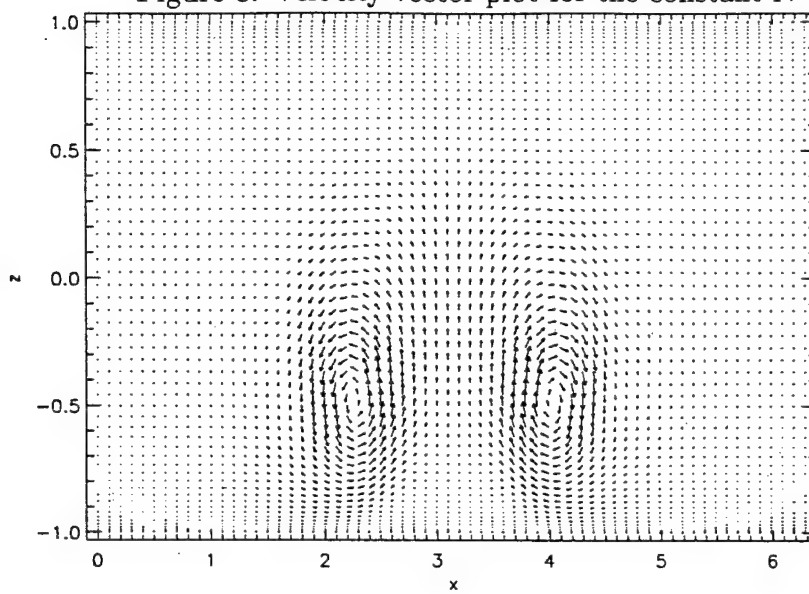


Figure 9: Velocity vector plot for the constant N case with $t=18.0$

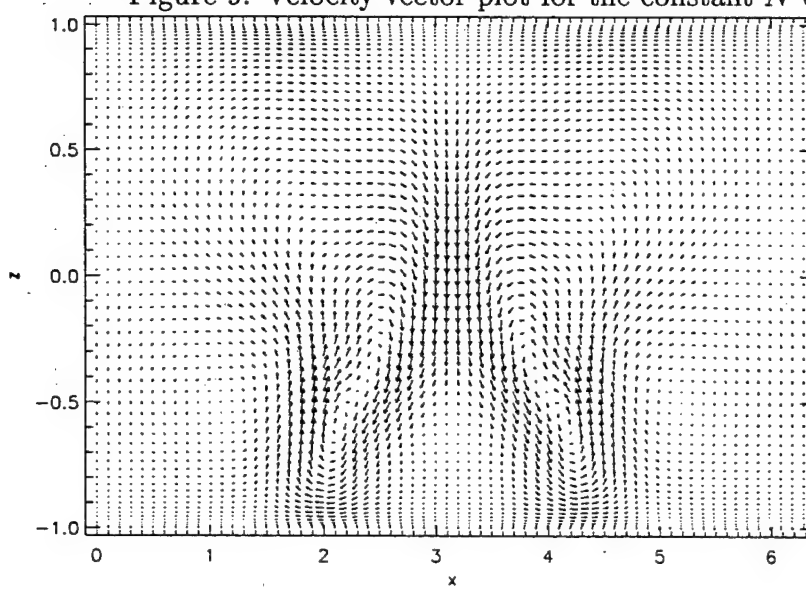


Figure 10: Velocity vector plot for the constant N case with $t=25.0$

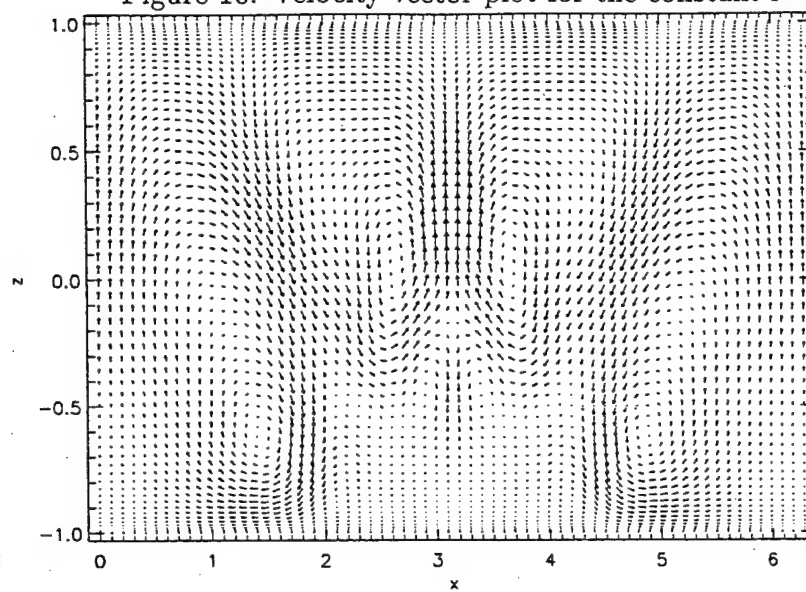


Figure 11: Velocity vector plot for the constant N case with $t=32.0$

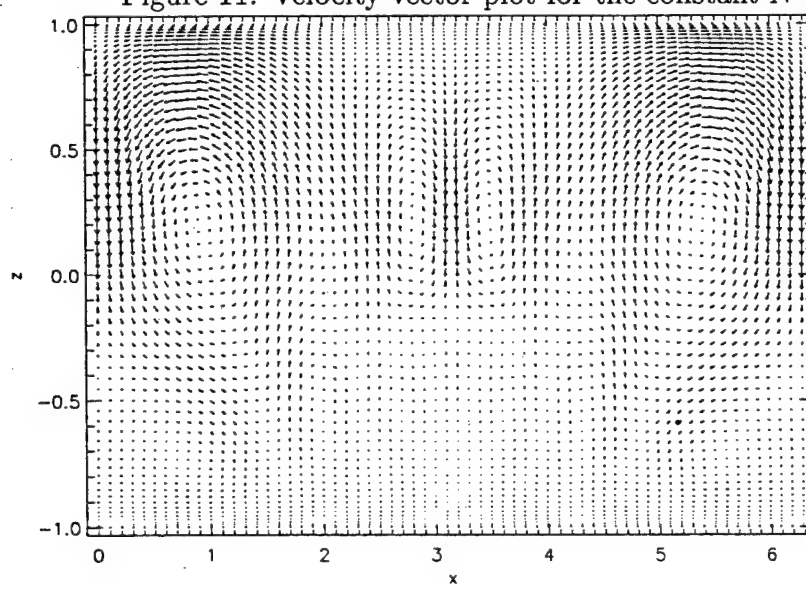


Figure 12: Surface plot of velocity magnitude for the constant N case with $t=1.0$

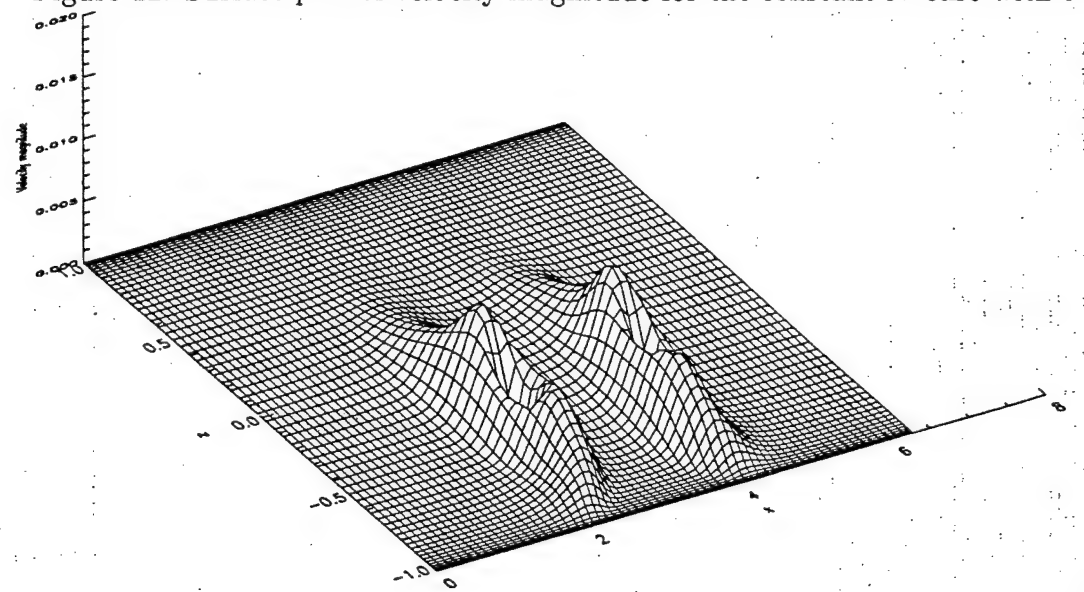


Figure 13: Surface plot of velocity magnitude for the constant N case with $t=18.0$

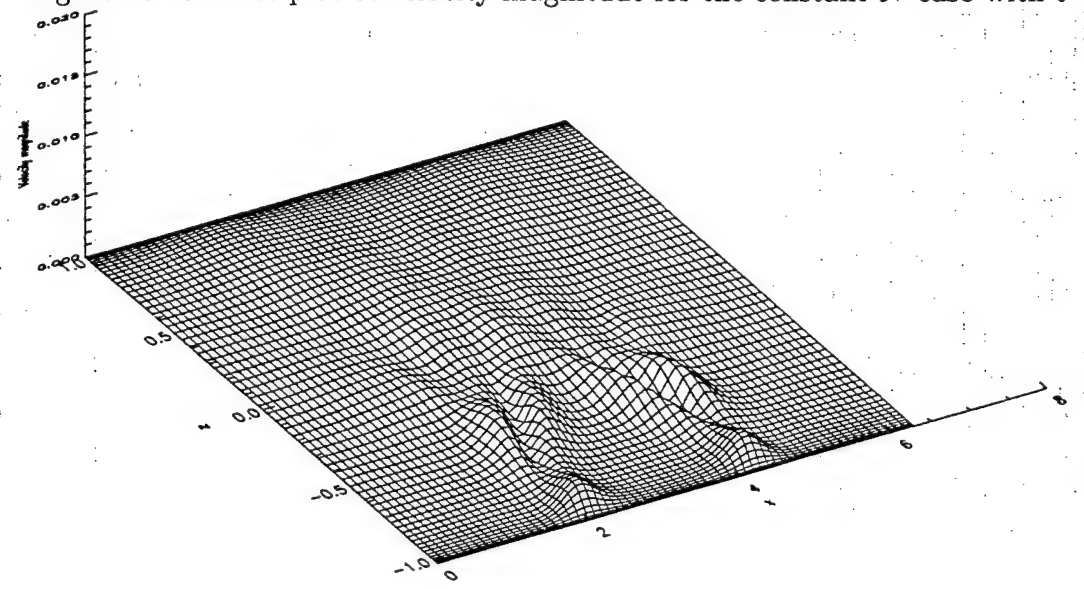


Figure 14: Surface plot of velocity magnitude for the constant N case with $t=25.0$

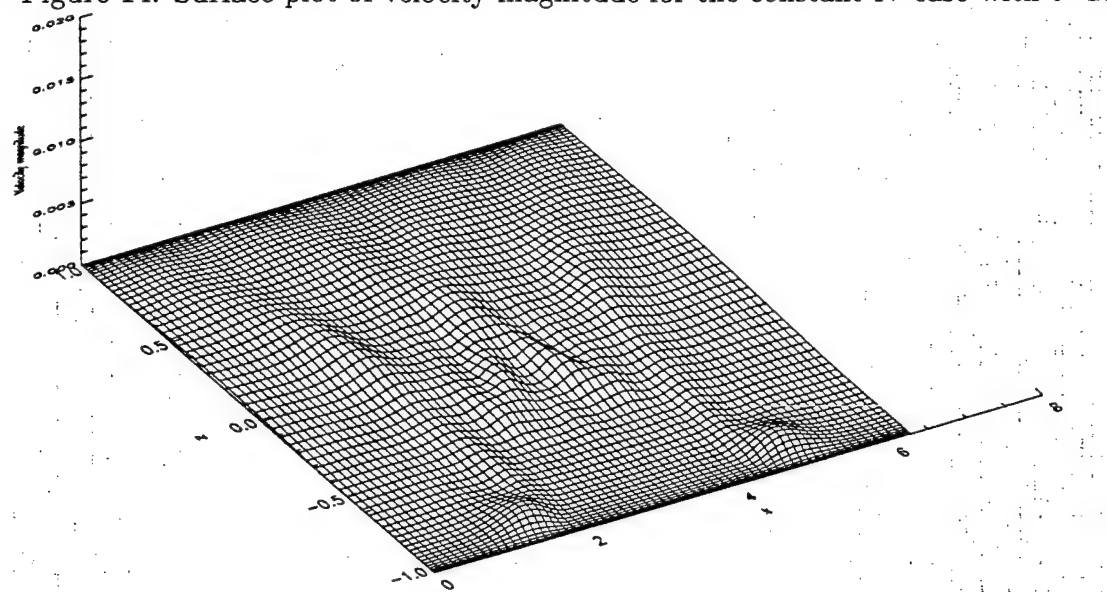


Figure 15: Surface plot of velocity magnitude for the constant N case with $t=32.0$

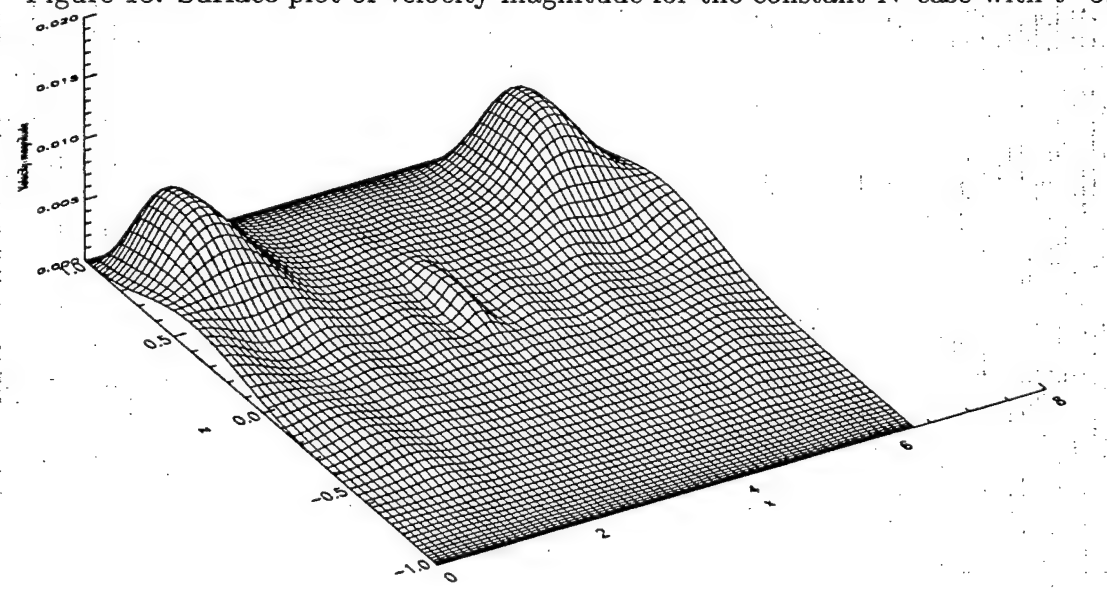


Figure 16: Contour plot of vorticity for the constant N case with $t=1.0$

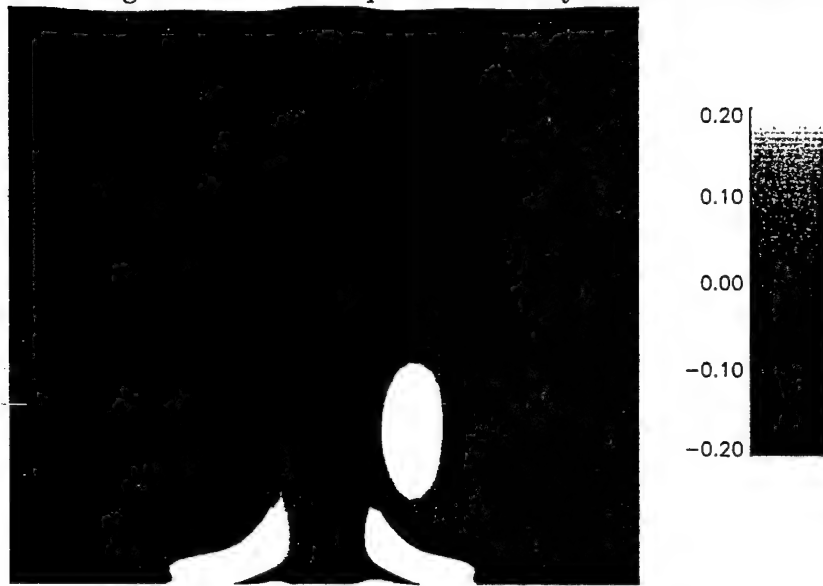


Figure 17: Contour plot of vorticity for the constant N case with $t=18.0$

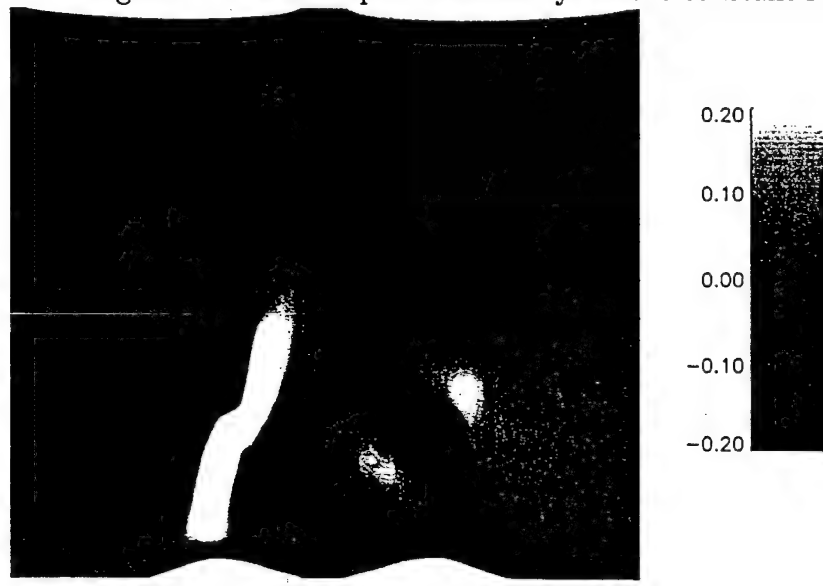


Figure 18: Contour plot of vorticity for the constant N case with $t=25.0$

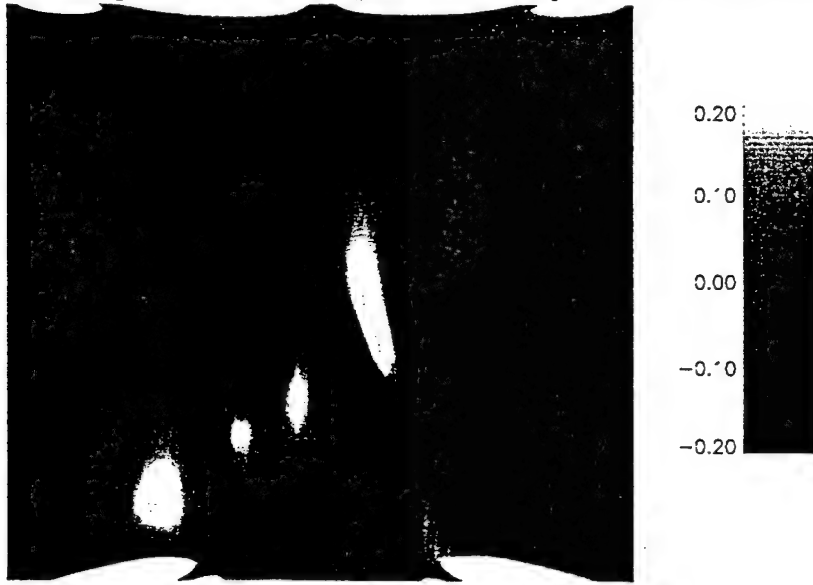
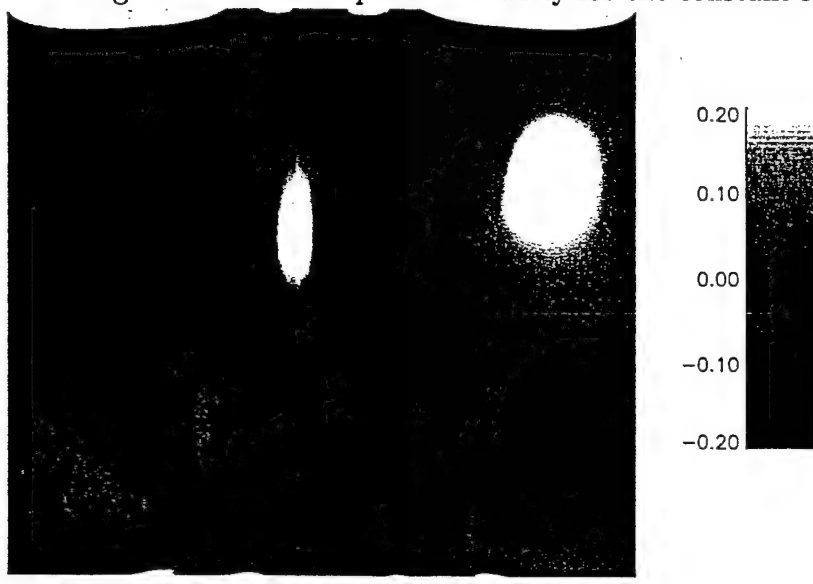


Figure 19: Contour plot of vorticity for the constant N case with $t=32.0$



constant density case. As soon as the vortices are released in the stratified flow, they very rapidly lose virtually all of the kinetic energy, as shown in figures 12-15. The surface plot in figure 12 clearly shows the two initial vortices, although they have decayed somewhat when compared to the surface plot for the constant density case at the same time, shown in figure 1. However, the coherency of the vortices disappears very quickly, and is replaced with an internal wave pattern, as shown in figures 13-15. This conversion of energy in the vortices into wave energy occurs in approximately one Brunt-Vaisala period,

$$\tau = \frac{2\pi}{N}, \quad (37)$$

defined as the time for one oscillation at the Brunt-Vaisala frequency, and has a dimensionless value of approximately 9.8 for the chosen Brunt-Vaisala parameter value of 0.32. The wave motion continues, and the initial vortex pair is never reformed. Interaction with the damping layer at the top, and viscous dissipation, finally cause the wave action to decay to zero.

It should be noted that the motion, initially symmetric about the vertical center of the domain, retains this symmetry during the entire simulation. Clearly the waves propagate rapidly to the sidewalls, and interact with the motion on the other side. Since the sidewalls are periodic, one may think of an identical motion on each side of the domain, evolving simultaneously. The results are therefore also symmetric about the vertical sidewall, and when wave energy impinges the sidewall, it is perfectly reflected due to this symmetry. This effect does not model the real atmosphere, although the solutions are accurate and satisfy all equations and boundary conditions. The results presented here focus on the motion before this reflection occurs.

Figures 5-6 show the time evolution of the vorticity for the constant density case. The initial vortices retain their identity, but dissipate, elongate, and move together and upwards. Note that the vorticity field is antisymmetric, and the dark and bright spots are due to the counterrotating nature of the vortex pair.

Figure 16 shows the vorticity contours for the stratified case after a mere ten time steps, and clearly the vortices are still coherent, and nearly identical to figure 5. Figure 17 shows two streaks of vorticity after an elapsed dimensionless time of

18, corresponding to the time for several oscillations at the Brunt-Vaisala frequency. Also evident in figure 17 are several other dark and bright spots of vorticity, in the vicinity of the streaks. The initial vortices do *not* evolve into these dark and light streaks, as one might assume. Instead, the initial vortices are now the small patches of vorticity visible on the outside of the larger streaks. The streaks of vorticity have been generated by the appearance of an internal wave motion, beginning to dominate the flow pattern. If the vorticity patches from the initial conditions are tracked, they are found to disappear within a time equivalent to three oscillations at the Brunt-Vaisala frequency. The motion of the vortex center is nearly horizontal, and moving away from the domain center.

Figures 18 and 19 are later time slices of the vorticity, showing regular patterns of positive and negative vorticity. These patterns indicate wave motion, rather than any historical result of the initial vortices. It is interesting to note in figure 19 that two intense patches of vorticity appear near the upper corners of the domain, approximately equal in strength to the original vortex. These patches appear as the wave motion reaches its greatest amplitude, as can be seen in figures 12-15, which are surface plots of the magnitude of the velocity at times corresponding to figures 16-19. This wave is not breaking, meaning the vertical gradient of potential temperature is a stable gradient, and the flow at this Reynolds number is not unstable. Yet one wonders if this motion at other parameter values could result in a Helmholtz shear type instability near the wave crest, and a resulting patch of turbulence.

The third base state is a two layer case, with constant Brunt-Vaisala frequency in each layer. The interface between layers is located at the vertical center of the domain. Figure 7 shows the base state density profile for this case, as well as the previous case. The parameter values are identical to the second case, except now the upper half of the domain has a Brunt-Vaisala parameter value of 0.62, corresponding to a Brunt-Vaisala frequency of 0.02 1/s, typical of the stratosphere.

The results of the two-layer case are shown in figures 20 through 31, using the same time values and graphics as the constant N case. The dynamics of the atmosphere for this two layer case is very similar to the single layer of constant N . The vortices lose coherency very quickly and form an internal wave pattern. The amplitude of

the waves in the upper layer for this two layer case are generally greater than the amplitude in the one layer case. This increase in amplitude is due primarily to the lower density at the higher elevations, rather than any dynamic effect at the interface of the two layers. Note that the waves in the upper layer reach a maximum amplitude more quickly compared with the single layer case.

Perhaps the most significant difference is evident in the contour plots, figures 28-31. Figure 28 shows the vorticity after a mere 10 time steps, and should be compared with figure 16, the vorticity contours for the single layer case at the same time. The vorticity with two layers at this early stage is nearly identical to the single layer, except at an elevation just above the interface between the two layers. A narrow strip with high levels of vorticity appears, as evident in figure 28. The dynamics in figure 28 are not yet dominated by internal waves, but the sudden change in Brunt-Vaisala frequency is clearly generating a layer of motion with enhanced vorticity.

Figure 29 shows that this layer of enhanced vorticity has evolved and generated two spots of strong vorticity, in addition to the spots and streaks of vorticity that existed with a single layer shown in figure 17. Except for this new layer of vorticity just above the interface of the two layers, the vorticity pattern matches the single layer case rather closely.

Figures 30 and 31 show the vorticity contours for the time values corresponding to the single layer case, shown in figures 18 and 19. Below the interface, the dynamics of the two layer case appear nearly identical to the single layer case. Above the interface, where the Brunt-Vaisala parameter is much different, the wave motion evolves on a different time scale. But the basic motion is similar. This is evident by the strong spots of vorticity, appearing at a time of 32 for the single layer case, but near a time of 25 for the two layer case. In fact the basic patterns of vorticity above the interface between figure 19 and figure 30 compare rather well, considering the time difference between the two figures.

The dispersion of energy from the original vortices is difficult to quantify, since the vortices become so ill-defined in a very short time. However, the flux of energy across a horizontal plane is a quantity indicative of the flux from the original vortex, and provides information concerning the later dynamics of the waves. Figure 39 shows the

Figure 20: Velocity vector plot for the two layer case with $t=1.0$

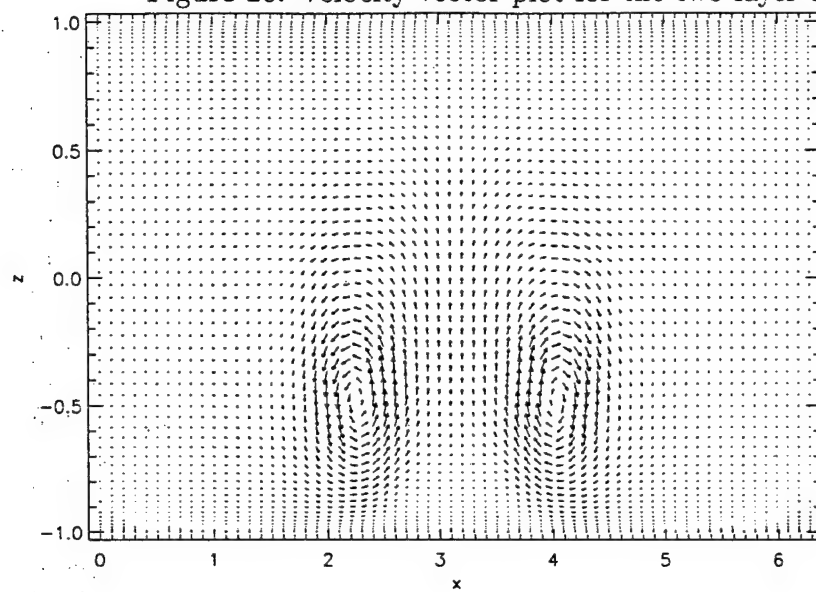


Figure 21: Velocity vector plot for the two layer case with $t=18.0$

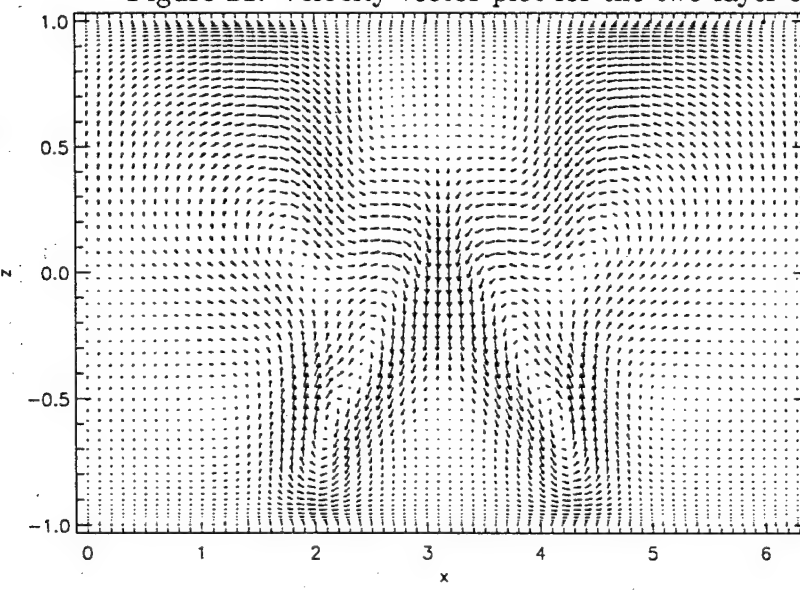


Figure 22: Velocity vector plot for the two layer case with $t=25.0$

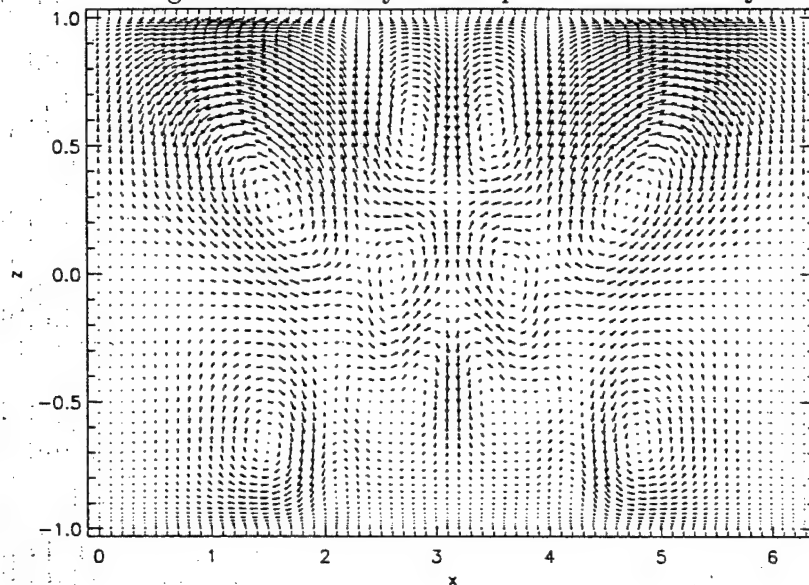


Figure 23: Velocity vector plot for the two layer case with $t=32.0$

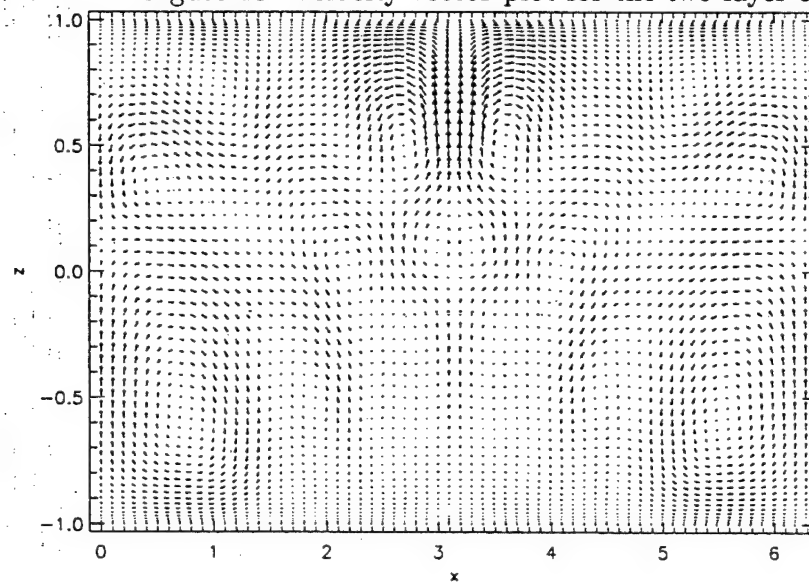


Figure 24: Surface plot of velocity magnitude for the two layer case with $t=1.0$

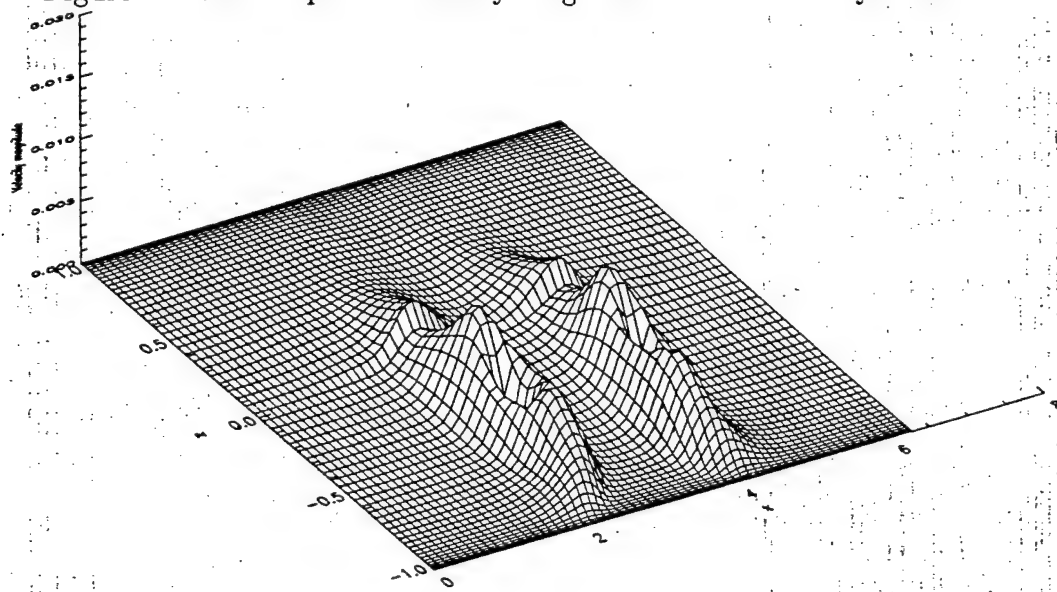


Figure 25: Surface plot of velocity magnitude for the two layer case with $t=18.0$

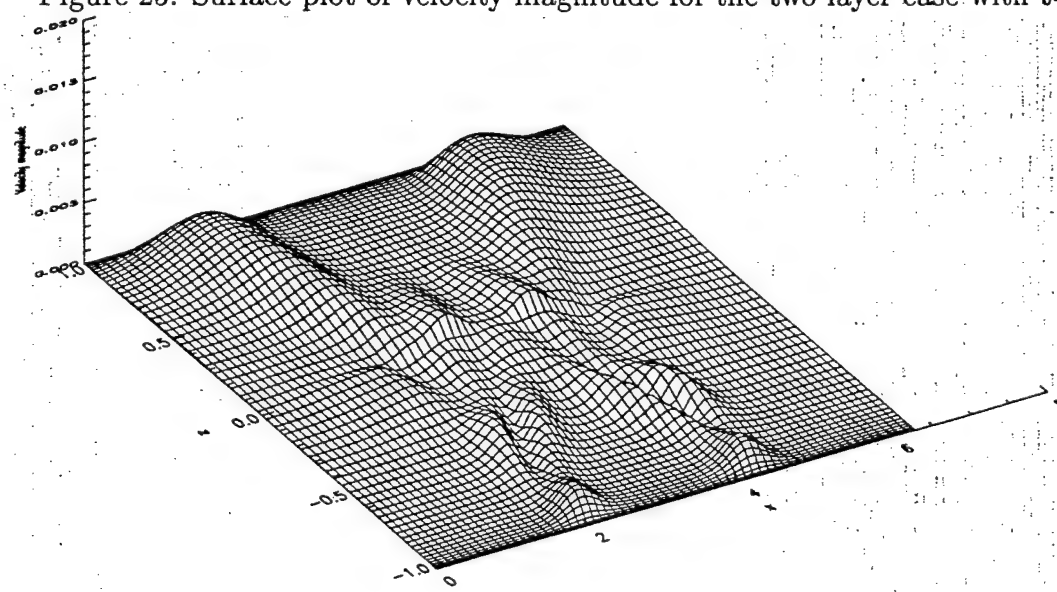


Figure 26: Surface plot of velocity magnitude for the two layer case with $t=25.0$

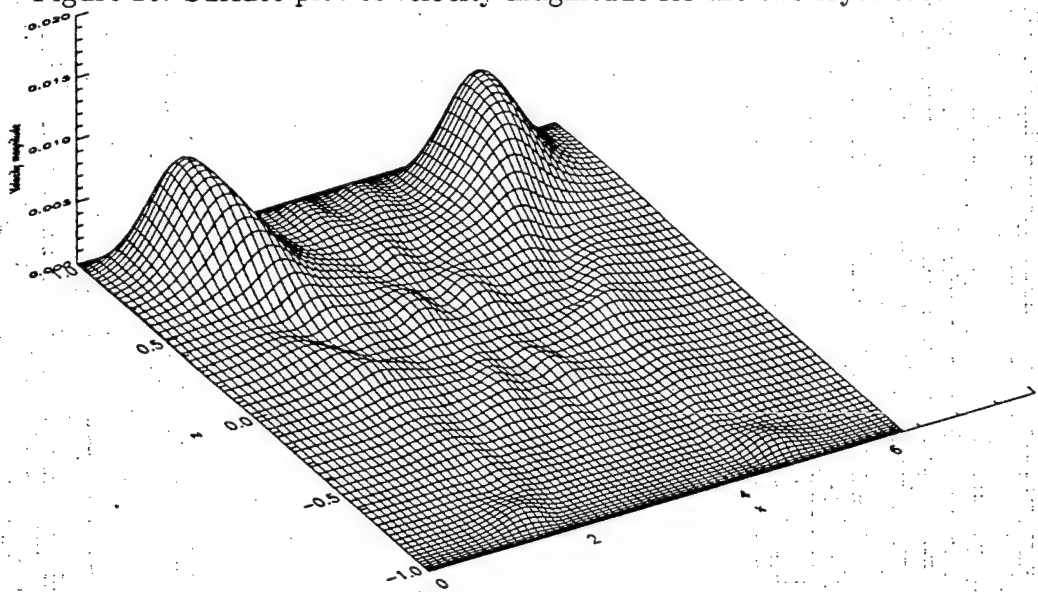


Figure 27: Surface plot of velocity magnitude for the two layer case with $t=32.0$

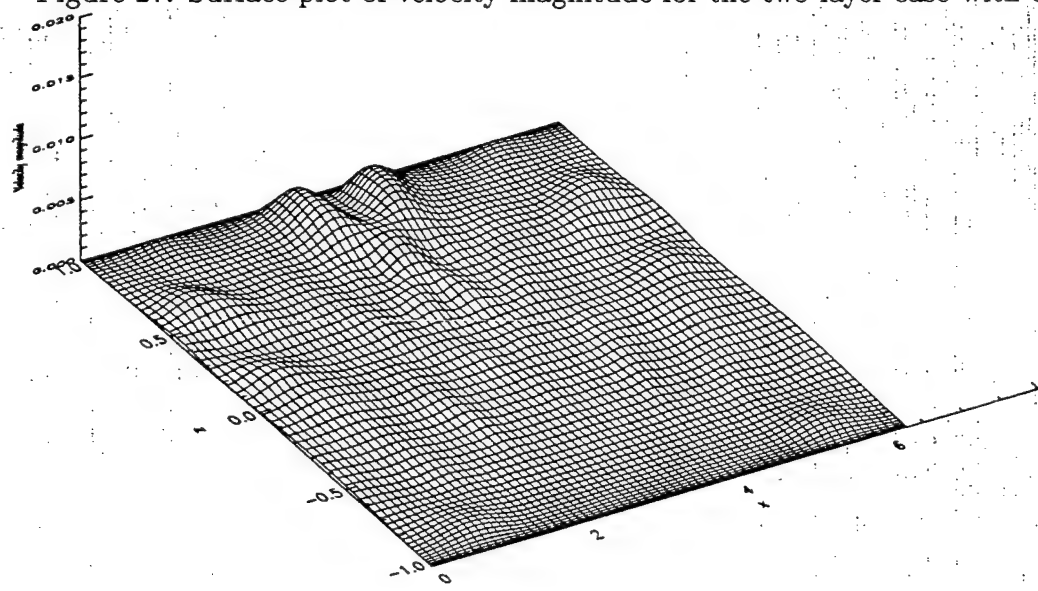


Figure 28: Contour plot of vorticity for the two layer case with $t=1.0$

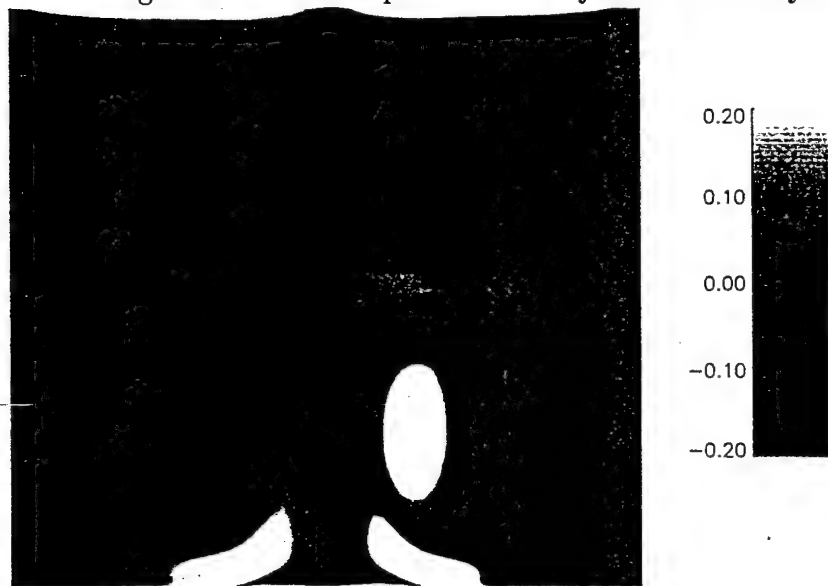


Figure 29: Contour plot of vorticity for the two layer case with $t=18.0$

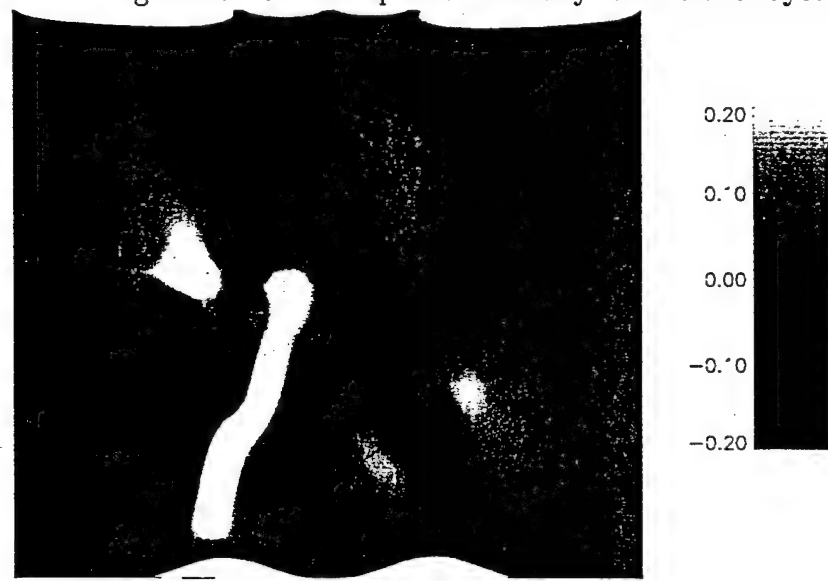


Figure 30: Contour plot of vorticity for the two layer case with $t=25.0$

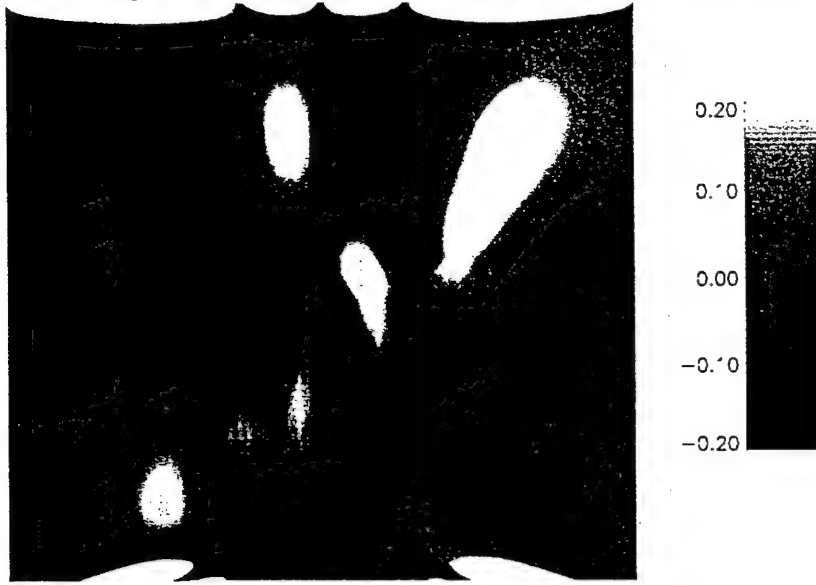
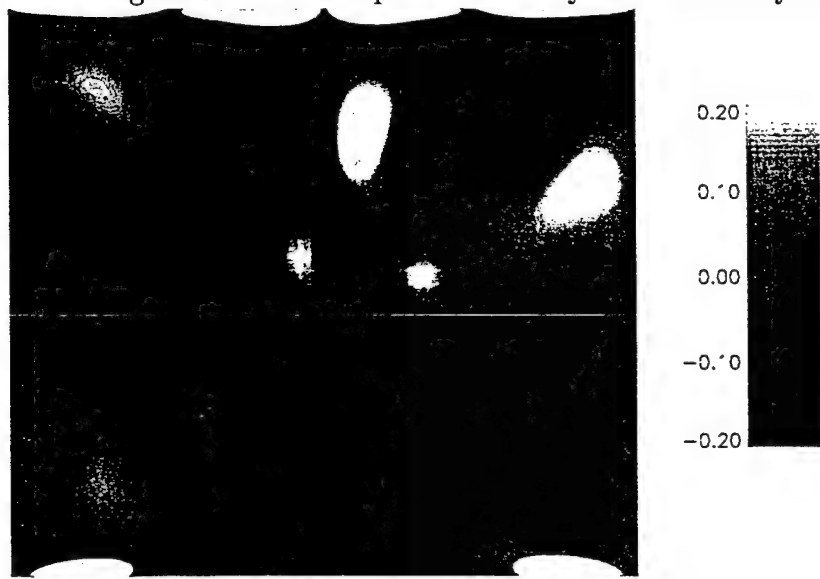


Figure 31: Contour plot of vorticity for the two layer case with $t=32.0$



temporal evolution of the vertical energy flux for all three base states, where vertical energy flux is defined as

$$E_w = \overline{w(u^2 + w^2)}, \quad (38)$$

and the overline represents a horizontal average. The value shown in figure 39 corresponds to the energy flux across the vertical center of the domain.

The value of E_w for the constant density case starts out negative, as shown in figure 39, due to the strong downdraft in the region between the two vortices. As the vortices move upward, this energy flux gradually becomes positive and then stops increasing as the position of the center of the vortices approaches the vertical center of the domain.

The value of E_w for the stratified cases are also shown in figure 38. Note the dramatic difference between the constant density case and the stratified cases. The single layer case very quickly shows large positive values of E_w , associated with the rapid transfer of vortical energy to wave energy. Then a very large negative energy flux occurs. This negative energy flux is associated with the complicated wave motion in the region between where the original vortices were located. This effect occurs before the elapsed time has reached even one Brunt- Vaisala period, and before any significant energy has reached the boundaries. The remainder of the data shows some oscillations, centered around zero energy flux. The flow beyond a time of approximately 32 is likely to be affected by reflected waves off the sidewalls. Hence, the later wiggles in figure 38 may not be indicative of motion in a real nonsymmetric atmosphere. The energy flux for the two layer case is very similar to the single layer case. The rate of decay of the energy flux as the initial positive value changes to a negative value is nearly identical.

Another measure of energy transfer is the temporal evolution of the total kinetic energy, defined as

$$E = \int_V \rho(u^2 + v^2) dV, \quad (39)$$

and is shown in figure 39, again for all three base states. The constant density case shows a rather slow exponential energy decay. This energy decay is clearly the result of viscous dissipation. Both stratified cases show much faster energy decay initially,

Figure 32: Vertical energy flux

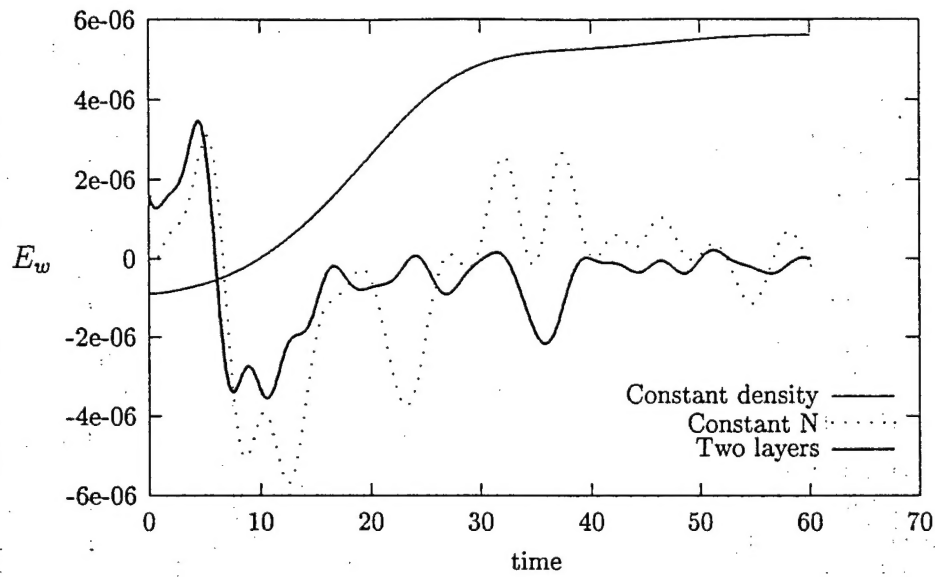
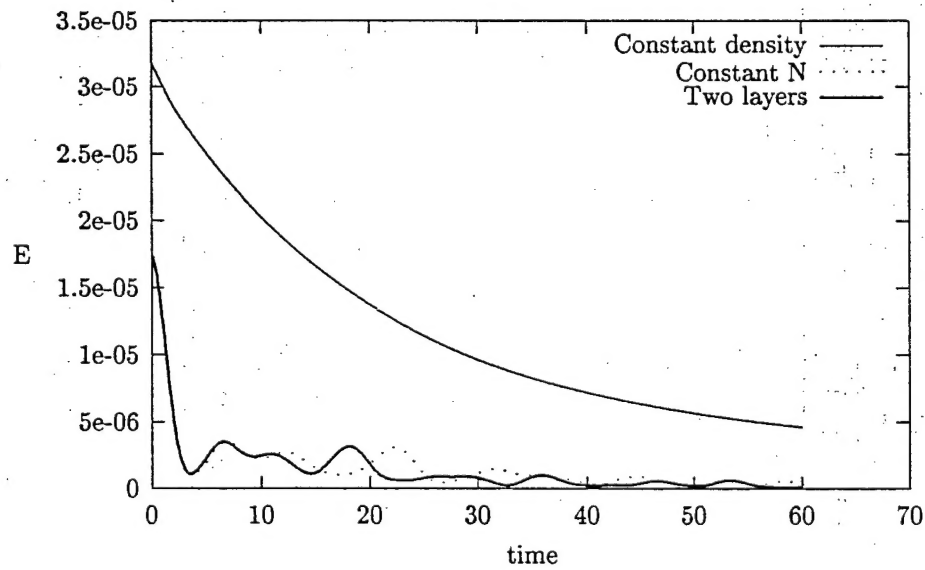


Figure 33: Total energy



followed by an oscillatory but gradual decay. This enhanced decay rate is caused by waves rapidly transporting energy away from the vortices, finally reaching the upper boundary where the energy 'escapes' by being absorbed by the damping layer.

6 Conclusions

Several conclusions can be drawn:

1. A vortex pair in a strongly stratified fluid rapidly loses energy to internal wave motion.
2. The original vortices move horizontally, instead of the vertical motion in a constant density flow.
3. The narrow region above the interface between layers of constant Brunt-Vaisala frequency experiences an enhanced level of vorticity during the motion.

Acknowledgement

Funding for one author (GSL) was provided by AFOSR through the Air Force Geophysics Scholar program. Funding for the other author (JPM) was provided by AFOSR through Hanscom AFB. Calculations were performed at the NAVO High Performance Computing Center.

References

- [1] E. Dewan, R. Picard, R. O'Neil, H. Gardner, J. Gibson, J. Mill, E. Richards, M. Kendra, W. Gallery, "MSX satellite observations of thunderstorm-generated gravity waves in mid-wave infrared images of the upper stratosphere," *Geophysical Research Letters*, **25**, pp. 939-942, 1998.
- [2] T. L. Clark, T. Hauf, J. P. Kuettner, "Convectively forced internal gravity waves: Results from two-dimensional numerical experiments," *Quarterly Journal of the Royal Meteor. Society*, **112**, pp. 899-925, 1986.

- [3] T. P. Lane, M. J. Reeder, and T. L. Clark, "Numerical modelling of gravity wave generation by deep tropical convection," Department of Mathematics Report #99/12, Monash University, 1999.
- [4] R. Fovell, D. Durran, and J. R. Holton, "Numerical simulations of convectively generated stratospheric gravity waves," *Journal of the Atmospheric Sciences*, **49(16)**, pp. 1427-1442, 1992.
- [5] J. R. Holton and M. J. Alexander, "Gravity waves in the mesosphere generated by tropospheric convection," *Tellus*, **51A-B**, pp. 45-58, 1999.
- [6] F. M. Hill, "A numerical study of the descent of a vortex pair in a stably stratified atmosphere," *Journal of Fluid Mechanics*, **71**, pp. 1-13, 1975.
- [7] G. K. Batchelor, "The condition for dynamical similarity of a frictionless perfect-gas atmosphere," *Quarterly Journal of the Royal Meteor. Soc.*, **79**, pp. 224-235, 1953.
- [8] Y. Ogura and N. A. Phillips, "Scale analysis of deep and shallow convection in the atmosphere," *Journal of Atmospheric Science*, **19**, pp. 173-179, 1962.
- [9] R. Wilhelmson and Y. Ogura, "On the pressure perturbation and the numerical modeling of a cloud," *Journal of Atmospheric Science*, **29**, pp. 1295-1307, 1972.
- [10] F. B. Lipps and R. S. Hemler, "A scale analysis of deep moist convection and some related numerical calculations," *Journal of Atmospheric Science*, **39**, pp. 2192-2210, 1982.
- [11] J. T. Bacmeister and M. R. Schoeberl, "Breakdown of vertically propagating two-dimensional gravity waves forced by orography," *Journal of Atmospheric Science*, **46**, pp. 2109-2134, 1989.
- [12] J. McHugh, "An implicit algorithm for the anelastic equations," submitted.

- [13] J. Kim, P. Moin, and R. Moser, "Turbulent statistics in a fully developed channel flow at low Reynolds number," *Journal of Fluid Mechanics*, 177, pp. 133-166, 1987.
- [14] F. S. Sherman, *Viscous Flow*, McGraw-Hill, Inc., 1990.
- [15] H. Lamb, *Hydrodynamics*, Cambridge University Press, 1932.